Surface Structure of Epitaxial Magnetite $Fe_3O_4(001)$ Films: In Situ STM and CEMS Studies†

Nika Spiridis,‡ Bartosz Handke,‡ Tomasz Slezak,§ Jakub Barbasz,‡ Marcin Zajac,§ Jerzy Haber,*,‡ and Jozef Korecki‡,§

Institute of Catalysis and Surface Chemistry, Polish Academy of Sciences, Niezapominajek 8, 30-239 Kraków, Poland, and Faculty of Physics and Nuclear Techniques, AGH University of Science and Technology, Al. Mickiewicza 30, 30-059 Kraków, Poland

Received: January 6, 2004; In Final Form: April 6, 2004

Epitaxial $Fe_3O_4(001)$/MgO(001) films obtained by reactive molecular beam epitaxy were studied using a combination of in situ scanning tunneling microscopy (STM) and monolayer ^{57}Fe probe Conversion Electron Mössbauer Spectroscopy (CEMS). For the as-grown films the $(\sqrt{2} \times \sqrt{2})$R45° surface reconstruction was observed in agreement with the earlier studies. UHV annealing considerably improves the films' surface quality (the lateral size of the terraces) but it inevitably leads to the diffusion of magnesium into the magnetite film resulting in pronounced changes of the surface structure as seen in LEED and STM. Correlation of the STM and CEMS data indicates a more complicated surface termination than the homogeneous octahedral or tetrahedral one. A charge redistribution in the surface layer evidenced by CEMS can be responsible for the surface reconstruction. Despite the surface structural and electronic modification, the presence of the Verwey transition in the surface layers is proved by low-temperature CEMS.

1. Introduction

Epitaxial magnetite films are intensively studied for their potential catalytic and spintronic applications.[1,2] However, many features of their structural, electronic, and magnetic properties are still under debate. Among them one of the most controversial is surface termination and reconstruction, whose complication reflects complexity of the bulk magnetite crystallographic and electronic structure. Magnetite crystallizes in the cubic inverse spinel structure with the lattice constant of 0.843 nm. The oxygen ions form a close-packed cubic structure with Fe ions localized in two different interstitial sites, octahedral and tetrahedral. The 64 tetrahedral sites (A) in the unit cell are occupied by 8 trivalent Fe ions. Due to electron hopping, 16 tri- and divalent Fe ions occupying 32 octahedral sites (B) are randomly arranged at room temperature. At $T_V \sim 125$ K a metal−insulator transition, known as the Verwey transition, takes place. The common interpretation of the Verwey transition is the freezing of the electron hopping accompanied by a long range electron charge ordering in the octahedral Fe sublattice. It was also postulated that the Verwey transition at the surface might take place at considerably higher temperature,[3,4] which could also contribute to the surface magnetite structure at room temperature. Surface termination and reconstruction of magnetite is a controversial problem. The surface structure of (001) oriented magnetite is usually discussed considering the bulk unit cell as composed of eight atomic sublayers, which contain either only tetrahedral iron atoms in A sites (the so-called A-layer) or oxygen and octahedral B iron ions (the so-called B-layer). The distance in the A−A or B−B layers is about 0.21 nm, whereas the smallest interlayer (A−B) spacing is about 0.11 nm. None of the bulk terminated $Fe_3O_4(001)$ surfaces (neither A nor B) is charge compensated and the charge neutrality condition of the polar $Fe_3O_4(001)$ is quoted as the driving force of the reconstruction. The reconstruction, although intensively studied with different methods for single crystals[5,6] as well as for epitaxial films,[7−12] is still not fully understood and explained. All previous STM studies of magnetite thin films on MgO-(001) were done ex situ, which requires a single crystalline-like handling of the surface (an ion bombardment combined with an annealing treatment in O_2) for restoring the surface cleanness.[9,12−14] In this paper we present results of the in situ STM and Conversion Electron Mössbauer Spectroscopy (CEMS) studies of $Fe_3O_4(001)$ epitaxial films obtained by reactive MBE. The presented STM result is representative for all of about 10 investigated samples.

2. Experimental Details

Samples were obtained on MgO(001) substrates cleaved in an N_2 atmosphere prior to the introduction into the UHV systems (base pressure below 1×10^{-10} mbar). The $Fe_3O_4(001)$ films with thickness between 20 and 40 nm were grown by Fe-vapor deposition in the presence of oxygen at the rate of about 1 nm/min, on the substrate held at 250 °C. After the deposition of iron was completed, the oxygen admission was stopped but the sample temperature was kept at 250 °C for about half an hour. The STM images were acquired using the Aris1100 (Burleigh) STM head and electrochemically etched W-tips. The Mössbauer spectra were measured in situ in another multi-chamber UHV system[15] by detection of the conversion and Auger electrons following the recoilless nuclear absorption. The sample was mounted to the standard holder fixed to a coldfinger of a stationary liquid nitrogen cryostat. A tungsten heater and a K-type thermocouple located near the sample allowed the measurements to be performed in the temperature range between 80 and 500 K. A specially designed (small active area) ^{57}Co

† Part of the special issue "Gerhard Ertl Festschrift".

* To whom correspondence should be addressed. Tel.: +4812 6395102, Fax.: +4812 4251923, E-mail: nchaber@cyf-kr.edu.pl.

‡ Polish Academy of Sciences.

§ AGH University of Science and Technology.

10.1021/jp049935i CCC: $27.50
Published on Web 06/22/2004

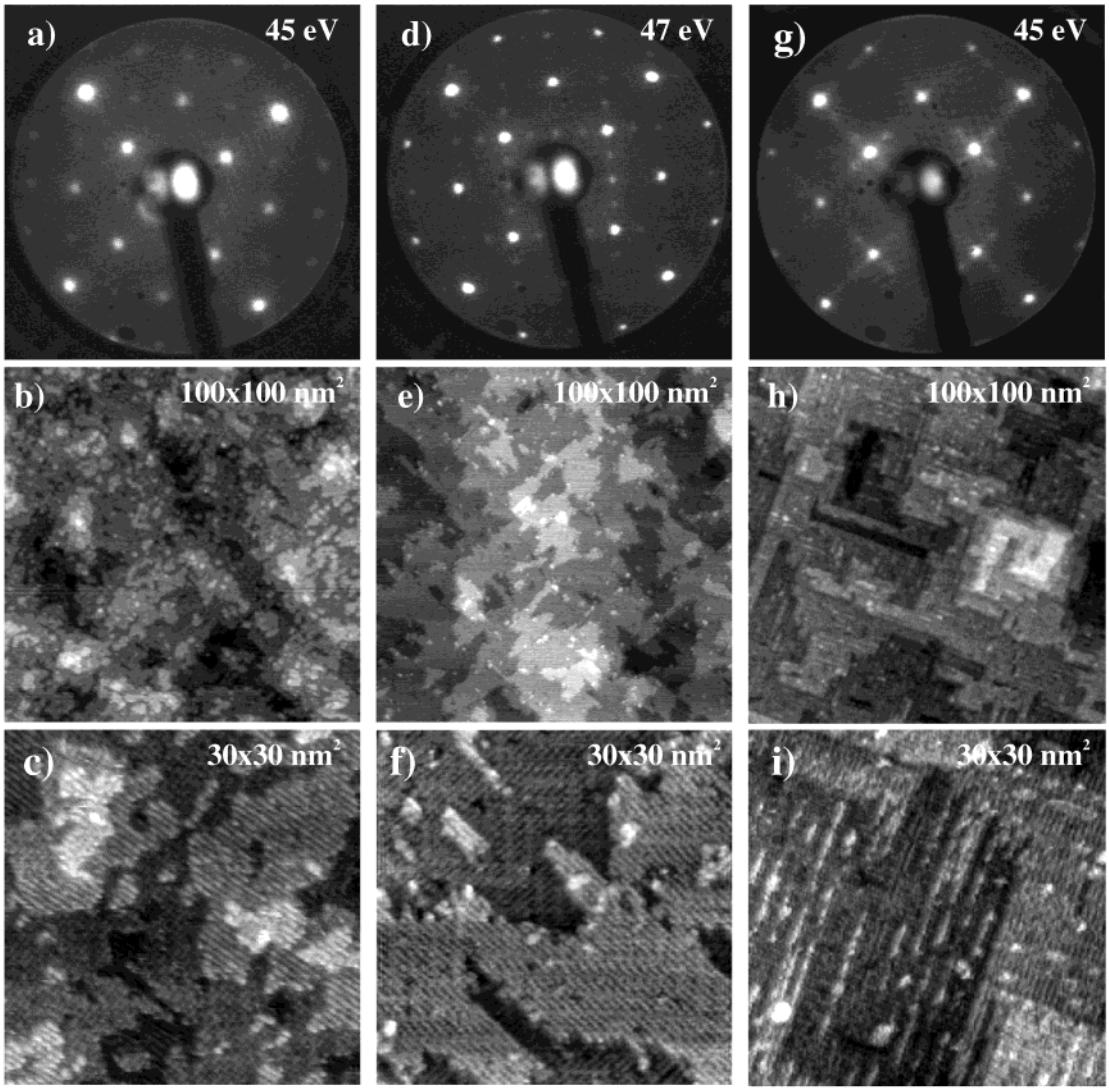

Figure 1. LEED patterns and STM images for the surface of an $Fe_3O_4(001)$ film deposited at 250 °C (a, b, c) and annealed at 380 °C (d, e, f) and 560 °C (g, h, i). STM images are taken at the sample bias voltage $V_s = +0.9 \pm 0.1$ V and tunneling current about 1 nA.

$\gamma-$source was placed outside the UHV system, inside a stainless steel tube entering the chamber. The tube was closed with a beryllium window transparent for the γ rays. The advantage of this solution is a small (3 cm) source-to-sample distance. The source was moved horizontally by a Mössbauer transducer fixed to the chamber. A large opening channeltron (25 mm diameter) placed a few millimeters from the sample was used to detect the conversion and Auger electrons resulting from the resonant absorption of the γ radiation in the sample. To avoid a signal from the sample holder, which can be also coated with ^{57}Fe during preparation, a movable shutter was used to limit the electrons to those that originated in the sample. Both the channeltron assembly and the Be-window tube can be retracted using edge-welded bellows, allowing the sample exchange.

The surface selectivity of the CEMS measurements could be enhanced by using an ultrathin ^{57}Fe surface probe layer on top of an ^{56}Fe film. During deposition of the ^{57}Fe probe layer the sample temperature was decreased to 150 °C to avoid ^{56}Fe/^{57}Fe intermixing.

3. Results and Discussion

3.1. LEED and STM. For the as-grown film the $(\sqrt{2} \times \sqrt{2})$R45° surface reconstruction corresponding to the 0.84 × 0.84 nm^2 surface unit cell is seen from LEED (Figure 1a), however the reconstruction spots are weak. It is the most typical reconstruction for MBE grown films monitored in situ by LEED or RHEED.[9−11] Surprisingly, in situ diffraction experiments were never combined with in situ STM studies. The in situ STM images corresponding to the LEED pattern from Figure 1a are shown in Figs 1b, c. In many details the images taken at the positive sample bias of about 1 V are very similar to those presented by Stanka et al.[12] for a thick (500 nm) film. On the larger 100 × 100 nm^2 scan (Figure 1b) irregular terraces are seen with the average step height of about 0.2 nm, which corresponds to the A−A or B−B layer spacing. The higher magnification (Figure 1c) shows that the terraces are composed of atomic rows spaced by 0.6 nm, which are mutually perpendicular on the neighboring terraces. Occasionally there are also areas where the row orientation changes within a terrace. According to the surface symmetry the rows are commonly interpreted as coming from Fe ions in octahedral sites. The rows can be perpendicular on a certain terrace due to stacking faults.[9,12] The atomically-resolved STM images taken at the positive sample bias showed a pronounced dependence on the tunneling conditions, which is presented in Figure 2. At a lower sample bias (Figure 2a, $V_s = 0.75$ V) the terraces become more diversified in height and additionally, very strong modulation of the intensity along the rows appears in some areas, forming

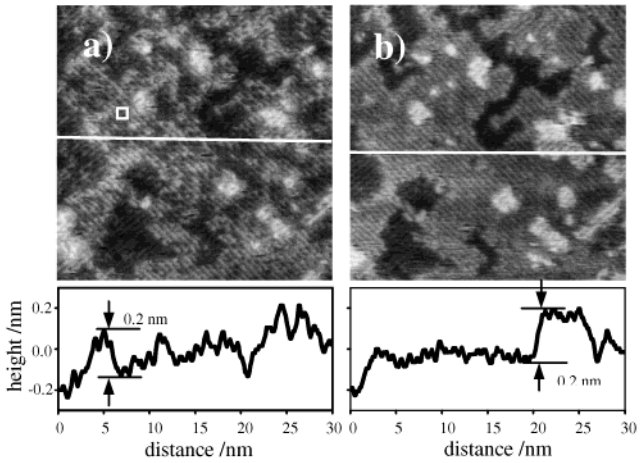

Figure 2. Bias dependence of the STM images for the surface of an $Fe_3O_4(001)$ film deposited at 250 °C. Images are taken at the sample bias voltage $V_s = +0.75$ V (a) and $V_s = +1$ V (b). The surface unit cell of the $(\sqrt{2} \times \sqrt{2})R45°$ reconstruction is marked in (a). Sections through the marked lines are shown below the images.

the structure of dark "holes" responsible for the $(\sqrt{2} \times \sqrt{2})R45°$ reconstruction. Many different reconstruction models based on A- or B-type layer termination were proposed and discussed in the literature − the most recent review can be found in the paper of Mijiritskii and Bjorma.[8] Nearly all models explaining the reconstruction of the $Fe_3O_4(001)$ surface emphasize that autocompensation is a necessary condition for the correctness of any particular surface structural model.[16] The most natural way to achieve autocompensated $Fe_3O_4(001)$ surfaces that possess the observed $(\sqrt{2} \times \sqrt{2})R45°$ symmetry is to terminate it with the not fully occupied layers: half-occupied tetrahedral Fe^{3+} monolayer for the A termination or a number of the oxygen vacancies for the B termination. However it must be pointed out that surface neutrality can also be achieved by the charge flow, because magnetite is a conductor.

Some authors believe that both types of termination are possible,[16] but the consensus is that they do not occur simultaneously on one surface. Such a conclusion comes from the STM images, in which the smallest step height observed on the $Fe_3O_4(001)$ surface is about 0.2 nm, which corresponds to the interplanar spacing of the A−A or B−B layers, whereas for the mixed A/B termination 0.1 nm steps corresponding to the A−B interlayer spacing are expected. The sections in Figure 2 indicate that the measured terrace height depends on the tunneling conditions. In the case of the bias voltage of 1 V the two monatomic terraces are spaced apart by 0.2 nm and only minor height modulation is seen for a given terrace, whereas the situation changes entirely when the bias voltage is lowered to 0.75 V. The terrace height becomes very diversified, a height difference up to 0.2 nm can be measured on the same terrace. Apparently, the simple model assuming a perfect termination with the full and homogeneous octahedral or tetrahedral layer does not apply for the small terraces with high defect densities, which are typical for the samples prepared at 250 °C. The important message from the STM measurements is that the as-prepared magnetite surface at the typical condition of the oxygen-assisted epitaxy (substrate temperature 250 °C) is much more inhomogeneous than commonly believed. By no means can such a preparation result in a perfect and well defined termination, as could be concluded from a diffraction pattern only displaying the $(\sqrt{2} \times \sqrt{2})R45°$ reconstruction.

The surface flatness can be improved by annealing, however the annealing at temperatures above 450 °C inevitably leads to the interdiffusion at the $Fe_3O_4(001)/MgO(001)$ interface[13] detectable by CEMS measurement.[17,18]

Our in situ LEED and STM results for annealed $Fe_3O_4(001)$ films are shown in Figure 1.d−i and in Figure 3.a, c. After annealing at 380 °C the reconstruction changes to $(2\sqrt{2} \times \sqrt{2})R45°$ (Figure 1.d−f). The details of the $(2\sqrt{2} \times \sqrt{2})R45°$ reconstruction are shown in Figure 3a. The two possible reconstruction domains are visualized by the rectangles representing the 0.84×1.68 nm^2 unit cells. The $(2\sqrt{2} \times \sqrt{2})R45°$ reconstruction is very stable and we were not able to restore the original $(\sqrt{2} \times \sqrt{2})R45°$ one by any thermal treatment at the UHV conditions. The appearance of this new reconstruction is not accompanied by any detectable changes of the CEMS spectra, as follows from our previous results, so it must be related to the outermost surface layer only, and apparently is not connected with diffusion of Mg from the substrate into the film. The same reconstruction can be obtained when deposition of the film is carried out at higher temperature; for example, at 330 °C. Figure 3b shows that a higher growth temperature makes the sample surface more homogeneous on a small scale but it increases the number of exposed terraces to about 10 as compared with four to five for a standard growth temperature of 250 °C. Our interpretation of the $(2\sqrt{2} \times \sqrt{2})R45°$ reconstruction is based on the assumption that the growth of magnetite takes place at a certain excess of oxygen, because the partial pressure of oxygen used for the preparation usually considerably exceeds the minimum pressure required to avoid formation of a wustite structure. Hence, the most probable and natural defects in the magnetite structure are iron vacancies in the octahedral sublattice. The concentration of the vacancies can be as high as 1/6 of the octahedral iron ions, which corresponds to the

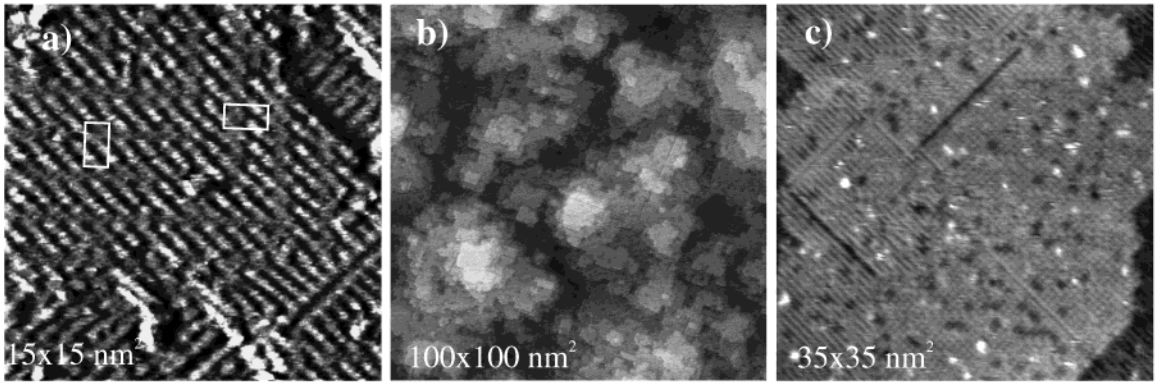

Figure 3. STM images for the surface of an $Fe_3O_4(001)$film: (a) after annealing at 380 °C showing details of the $(2\sqrt{2} \times \sqrt{2})R45°$ reconstruction, (b) deposited at 330 °C, and (c) after annealing at 500 °C.

composition of $\gamma-Fe_2O_3$.[7] By virtue of oxygen-assisted gas-phase growth, the highest concentration of the iron vacancies is expected at the surface. In this picture the reconstruction type would depend on the density and arrangement of the Fe vacancies in the octahedral surface layer. The annealing can produce a new reconstruction by an ordering of the iron vacancies. By simple geometrical arguments, the local concentration of the vacancies in the outermost B layer, which is necessary to produce the $(2\sqrt{2} \times \sqrt{2})$R45° reconstruction, is 1/8.

The LEED pattern for a sample annealed at 560 °C is shown in Figure 1g. The onset of a new (1×3) reconstruction that is typical for the Mg surface segregation[13] is also seen in LEED for samples annealed at 500 °C. The STM for that stage of annealing (Figure 3c) displays large and flat terraces with different atomic scale details. Atomic rows spaced by 0.6 nm, decorated with darker and brighter spots, dominate the images, which are however very sensitive to the bias voltage as could be expected for metallic Mg impurities on the oxide surface. The (1×3) reconstruction is revealed in the STM after 560 °C annealing (Figure 1h, i) as additional rows (spaced by 1.8 nm) that protrude from the surface along the ⟨110⟩ directions. These are probably Mg rich areas, forming nuclei of a surface $MgFe_2O_4$ compound.[13]

3.2. CEMS Results. Deeper insight into the problem of the composition and electronic structure of the surface layer was gained by the CEMS experiment. The Mössbauer spectroscopy has numerous advantages when applied to thin magnetite films. The method is crystal site and valency state sensitive and, additionally, by using ^{57}Fe probes[19] its spatial resolution can be enhanced into the monolayer range. The CEMS advantage in studying surface and interface properties of magnetite was convincingly demonstrated by Fujii et al.[20, 21] However, because they performed the CEMS experiment in air, the results cannot be taken as representative for the clean magnetite surface. Recently, Kalev et al.[22] reported an in situ emission Mössbauer experiment using ^{57}Co soft landed at surfaces and interfaces of epitaxial magnetite films providing information on the tetrahedral surface sites, which are preferentially occupied by the cobalt atoms.

The characteristic hyperfine pattern of magnetite reflected in the Mössbauer spectrum allows one to analyze the stoichiometry and cation distribution. As the reference we use the spectrum of a 400 nm epitaxial film. At room temperature, when the electron hopping process is fast, the Mössbauer spectrum of bulk-like magnetite is characterized by two sextets. The one with the hyperfine magnetic field $B_{hf} = 48.80(2)$ T and the isomer shift $IS = 0.269(1)$ mm/s relative to α−Fe corresponds to the $Fe^{3+}{}_A$ ions at the tetrahedral A-sites. The second one with $B_{hf} = 45.73(2)$ T and $IS = 0.654(1)$ mm/s is the $Fe^{2.5+}{}_B$-like average signal from the cations at the octahedral B sites. $Fe^{2+}{}_B$ and $Fe^{3+}{}_B$ are indistinguishable due to a fast electron transfer (electron hopping), which is faster ($\tau \sim 1$ ns) than the ^{57}Fe excited-state lifetime (98 ns). The magnetite unit cell contains 8 $Fe^{3+}{}_A$ ions and 8 $Fe^{2+}{}_B + 8\ Fe^{3+}{}_B$ ions, 16 in total at the B sites. Therefore, the intensity ratio $\beta = I(B)/I(A)$ of the two spectral components is a sensitive measure of the stoichiometry. Assuming that the room-temperature ratio of the recoil-free fractions f_B/f_A for the B and A sites is 0.94,[23] the intensity ratio β for perfect stoichiometry should be 1.88. In nonstoichiometric magnetite, under an excess of oxygen, cation vacancies at the B sites are created. The vacancies screen the charge transfer and freeze the hopping process. For each vacancy, five Fe^{3+} ions in octahedral sites become trapped. In the Mössbauer spectrum these trapped Fe^{3+} ions at the octahedral sites and Fe^{3+} ions at tetrahedral sites are indistinguishable without applying an external magnetic field. So, in the spectrum of nonstoichiometric magnetite, intensity transfer from the $Fe^{2.5+}{}_B$ to $Fe^{3+}{}_A$-like components is observed. Therefore, the intensity ratio β decreases markedly with the oxidation process, until the stoichiometry reaches the $\gamma-Fe_2O_3$ phase, which is represented by a single unresolved Zeeman component, close to that characteristic of the $Fe^{3+}{}_A$ site in magnetite.[7, 24]

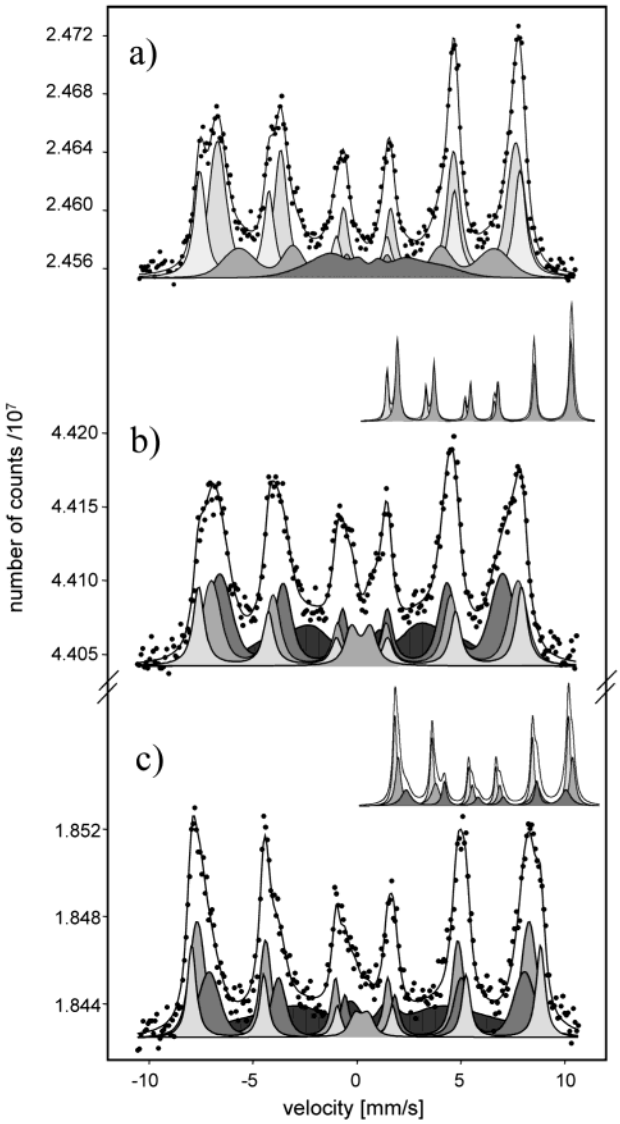

Figure 4. The CEMS spectra for 20 nm $^{56}Fe_3O_4(001)$ films with a surface $^{57}Fe_3O_4(001)$ probe layer of different thicknesses: (a) room-temperature spectrum for 0.7 nm, (b, c) room temperature and 85 K spectra, respectively, for 0.4 nm. Insets show the spectra for a 400 nm magnetite layer.

Our thick magnetite epitaxial films display the bulk-like Mössbauer spectra,[25] which are exemplified by the insets in Figure 4. To investigate surface effects, which were preliminarily reported earlier,[25] we have measured CEMS spectra for magnetite samples with ^{57}Fe surface probe layers with the thickness ranging from 2.4 to 0.4 nm. The thickness of the probe layers was estimated from the indication of the quartz balance with an accuracy of about 0.1 nm. Despite the prolonged spectra acquisition time (the whole measurement cycle for the thinnest probe layers took about four weeks), the surfaces of all samples preserved the $(\sqrt{2} \times \sqrt{2})$R45° reconstruction, indicating a minor contamination. Also, the partial spectra recorded every

TABLE 1: Fitted Hyperfine Parameters for the 20 nm $^{56}Fe_3O_4$(001) Films with the 0.7 and 0.4 nm $^{57}Fe_3O_4$(001) Surface Probe Layer Obtained from CEMS Spectra[a]

probe layer/temperature	spectral component	B_{hf} [T]	ΔB_{hf} [T]	*IS* [mm/s]	*QS* [mm/s]	relative intensity
0.7 nm/300K	C_A	47.9(1)	0.7(1)	0.302(5)	−0.04(1)	0.27(2)
	C_B	44.6(1)	1.72(5)	0.594(5)	−0.01(1)	0.47(3)
	S_1	38.2(3)	3.8(2)	0.583(5)	−0.01(1)	0.17(3)
	S_2	17.8(5)	7.2(5)	0.617(8)	−0.05(1)	0.09(1)
0.4 nm/300K	D			0.32(1)	0.45(4)	0.04(1)
	C_A	48.3(2)	0.4(1)	0.332(6)	−0.05(1)	0.16(2)
	C_B	45.8(2)	1.8(1)	0.441(6)	0.07(1)	0.25(2)
	S_1	42.3(3)	2.8(3)	0.430(5)	−0.09(1)	0.34(3)
	S_2	26.4(3)	7.6(4)	0.482(8)	−0.05(1)	0.21(2)
0.4 nm/85 K	D			0.34(1)	0.31(5)	0.02(1)
	C_{1-LT}	49.6(2)	1.6(1)	0.372(6)	0.03(1)	0.32(2)
	C_{2-LT}	52.2(1)	0.3(1)	0.524(7)	0.03(1)	0.17(2)
	C_{3-LT}	47.2(2)	2.5(2)	0.657(8)	−0.08(1)	0.23(2)
	S_{1-LT}	33.9(3)	14.2(8)	0.71(2)	−0.01(1)	0.26(2)
'Bulk'/300K (400nm)	A	48.80(2)		0.269(1)	0.00(1)	0.35(1)
	B	45.73(2)		0.654(1)	0.00(1)	0.65(1)

[a] B_{hf} is the hyperfine magnetic field and ΔB_{hf} is the width of its distribution, *IS* is the isomer shift and *QS* is the quadrupole splitting. *IS* values are given with respect to α-Fe. Parameters for a 400 nm film representing bulk magnetite at room temperature are given for comparison. Numbers in parentheses indicate the errors of the least-squares fit analysis.

24 h did not indicate any time evolution of the hyperfine pattern. It may be concluded that the influence of surface contamination (if any) saturated after the first measurement day.

The CEMS spectra for the 20 nm $^{56}Fe_3O_4$(001) films with the 0.7 and 0.4 nm ^{57}Fe surface probe layer measured at room temperature and for the 0.4 nm probe layer measured also at 85 K (below the Verwey transition) are shown in Figure 4. The results of numerical least-squares analysis represented by the solid lines are summarized in Table 1. All fits were made assuming Voigt lines and limiting the number of fitted parameters to the hyperfine parameters, their Gaussian distribution widths, and the spectral component intensities. The spectra of a 400 nm film (representing the bulk behavior) are also enclosed in Figure 4 for comparison.

Four and five spectral components had to be used to obtain a satisfactory fit for the 0.7 and 0.4 nm probe layers, respectively. In all fits the consistency within results for the probe layer of different thickness was secured. The nonmagnetic doublet (D) that was necessary only for the 0.4 nm probe layer can originate from the surface Fe atoms, which form hydroxide compounds observed at both temperatures. It has a very low intensity and will be omitted in the remaining discussion. Most of the spectral intensity is rather evenly distributed between four magnetically split spectral components. The increased number of the spectral components as compared to the bulk reflects the complexity of the electronic structure in the surface layers. In the first approximation, assuming a perfect termination, one could assign two of the components to the surface A and B layers and the other two to all deeper layers with the electronic properties not very different from the bulk. It has to be remembered that the B layers (containing octahedral Fe ions) contain double the amount of iron as compared to the tetrahedral A layer. The hyperfine parameters are good fingerprints of the specific crystallographic positions, except for unknown (specially for oxides) surface modifications. Consequently, for the room-temperature spectra (Figures 4a and 4b, Table 1), the component C_A can be clearly identified as originating from deeper, nearly perfect (bulk-like) tetrahedral Fe^{3+} A layers. Only the *IS* value is slightly increased as compared to the bulk (especially for the 0.4 nm probe layer). Deeper, subsurface octahedral B layers obviously contribute to the component C_B. The magnetic hyperfine field B_{hf} has the bulk value, whereas the isomer shift value is markedly reduced. The reduction of the *IS* for the component C_B means that the octahedral $Fe^{2.5+}$ cations in this layer are more Fe^{3+}-like, as they have lost their electron charge. The two discussed spectral components, C_A and C_B, have a narrower distribution ΔB_{hf} of the hyperfine magnetic field than the remaining two, in the logical agreement with their interpretation. The spectral contribution of these components corresponds to about 0.5 and 0.2 nm of the 0.7 and 0.4 nm probe layers, respectively. Thus, for both samples the remaining spectral intensities contributing to the surface components S_1 and S_2 originate from the layer of about 0.2 nm thickness.

The spectral components S_1 and S_2, identified as originating from the surface layers, cannot be described fully consistently for the two samples with different thicknesses of the probe layer, especially concerning the hyperfine magnetic field. It is understandable if one recalls the lower preparation temperature of the probe layers. The roughness and inhomogeneities are expected to increase with the growing thickness of the probe layer. Moreover, the hyperfine parameters are specific neither for octahedral nor for tetrahedral irons. The one with the smaller B_{hf}, S_2, might be regarded as being the true surface, because the modification of the hyperfine magnetic field is the most severe. Additionally, the very broad distribution of B_{hf} is the indication of a disorder in the arrangement of atoms contributing to this component.

Special attention should be paid to the thinnest probe layer of 0.4 nm as representing a true surface behavior. For this sample, both surface components have similar IS values that lie between those of octahedral and tetrahedral Fe. Without a doubt, the surface octahedral Fe ions have a formal ionic charge higher than those in bulk (they are more positive), whereas the tetrahedral ones show a tendency to lower their ionic charge. Such behavior is indicative of the charge neutralization of the polar Fe_3O_4(001) surface by a redistribution of the electrons in surface layers. Both octahedral and tetrahedral termination can be compensated in this way, so it is impossible to uniquely decide on the termination type. Our STM images revealed the pronounced inhomogeneity of the surface topography on the atomic scale. Similarly, from CEMS measurement it follows that the surface layer is composed of two atomic layers with octahedral and tetrahedral Fe ions subjected to a strong modification of the electronic properties.

The isomer shift can also be discussed in terms of the average values, which are independent of a fitting model as the isomer shift represents the spectrum center of gravity. The calculated

average isomer shift decreases from 0.538 mm/s for a thick (400 nm) film to 0.499 mm/s for the 0.7 nm surface layer and to 0.423 mm/s for the 0.4 nm surface layer, which is a clear indication of a changing average ionic character of the Fe ions toward the more electropositive. It is difficult to distinguish which of the crystal sites contribute to this effect because different mechanisms are possible depending on the surface termination. However, we note that the terminations, for which the surface charge neutrality is realized by missing surface ions (oxygen vacancies for octahedral termination or iron vacancies for the tetrahedral one), would not lead to a change of the cation valance state and hence of the isomer shift. Thus, we have a strong indication that the surface autocompensation is achieved by electronic and not geometrical degrees of freedom as postulated recently by Noguera.[26] This seems to be particularly favored for magnetite with its mixed valency.

Irrespectively of the surface structural and electronic modification, the appearance of the Verwey transition in the surface layers is evidenced by the low-temperature CEMS spectrum for the 0.4 nm probe layer (Figure 4c, Table 1). Qualitatively, the low-temperature spectrum is very similar to that of bulk magnetite. Even for bulk magnetite the Mössbauer spectrum below T_V becomes complicated and difficult to interpret due to structural phase transition and multiple twinning domains.[27] A simplified approach allows one to fit the spectrum with three components, corresponding to $Fe^{3+}{}_A$, $Fe^{2+}{}_B$, and $Fe^{3+}{}_B$, but such oversimplification leads to unrealistic cation distribution. Based on the simplest model, a clear interpretation can be given only to the C_{3-LT} component, which by the B_{hf} and IS values can be identified as originating from Fe^{2+} ions. The high B_{hf} components must be due to Fe^{3+} ions. The outermost surface iron ions contribute to the component S_{1-LT} with the broadest B_{hf} distributions.

4. Conclusions

The in situ STM images of the $Fe_3O_4(001)$ epitaxial films grown on MgO(001) at 250 °C, which displayed in LEED the $(\sqrt{2} \times \sqrt{2})R45°$ reconstruction, reproduce the main features observed earlier for the samples transferred through atmosphere.[12] However, based on the strong dependence of the images on the bias voltage, we postulate highly inhomogeneous termination: a defected octahedral layer with or without randomly distributed Fe^{3+} ions rather than the perfect octahedral termination with ordered oxygen vacancies or one-half of a tetrahedral A layer with ordered Fe^{3+} ions.

The $(\sqrt{2} \times \sqrt{2})R45°$ reconstruction obtained by annealing the film at temperatures up to 400 °C or in the case of films grown at a slightly higher temperature (330 °C) is more stable and we associate it with Fe vacancies in the surface octahedral layers. A further increase of annealing temperature leads to the surface segregation of Mg.

The electronic structure of the surface layers of magnetite is strongly modified as compared to the bulk. The CEMS results suggest a redistribution of the electronic charge in the two or three outermost atomic layers. The driving force of this process is autocompensation of the polar $Fe_3O_4(001)$ surface. The intensity of the spectral component, which can be associated with the $Fe^{2.5+}$ octahedral ions, is lower than could be expected from the estimation of the total amount of the octahedral Fe ions. Either the surface is enriched with Fe^{3+} ions (due to Fe vacancies in the octahedral sublattice) or it freezes the electron hopping, possibly introducing the charge ordering in the outermost octahedral layers. Such a mechanism could be responsible for the observed surface reconstruction as suggested recently by Mariotto et al.[28]

Acknowledgment. This work made in the frame of COST action D15 was partially supported by the Polish State Committee for Scientific Research, grant no. 7 T08A 002 20. Financial support by The Foundation for Polish Science (FNP) is kindly acknowledged.

References and Notes

(1) van der Zaag, P. J.; Bloemen, P. J. H.; Gaines, J. M.; Wolf, R. M.; van der Heijden, P. A. A.; van de Veerdonk, R. J. M.; de Jonge, W. J. M. *J. Magn. Magn. Mater.* **2000**, *211*, 301.

(2) Peden, C. H. F.; Herman, G. S.; Ismagilov, I. Z.; Kay, B. D.; Henderson, M. A.; Kim, Y.-J.; Chambers, S. A. *Catal. Today* **1999**, *51*, 513.

(3) Wiesendanger, R.; Shvets, I. V.; Bürgler, D.; Tarrach, G.; Güntherodt, H. J.; Coez, J. M. D.; Gräser, S. *Science* **1992**, *255*, 583.

(4) Koltun, R.; Herrmann, M.; Güntherodt, G.; Brabers, V. A. M. *Appl. Phys.* **2001**, *A73*, 49.

(5) Tarrach, G.; Burgler, D.; Schaub, T.; Wiesendanger, R.; Güntherodt, H.-J. *Surf. Sci.* **1993**, *285*, 1.

(6) Seoighe, C.; Naumann, J.; Shvets, I. V. *Surf. Sci.* **1999**, *440*, 116.

(7) Voogt, F. C. Ph.D. Thesis, Departments of Chemical Physics and Nuclear Solid State Physics, University of Groningen, Netherlands, 1998.

(8) Mijiritskii, A. V.; Boerma, D. O. *Surf. Sci.* **2001**, *486*, 73.

(9) Gaines, J. M.; Bloemen, P. J. H.; Kohlhepp, J. T.; Bulle-Lieuwma, C. W. T.; Wolf, R. M.; Reinders, A.; Jungblut, R. M.; van der Heijden, P. A. A.; van Eemeren, J. T. W. M.; aan de Stegge, J.; de Jonge, W. J. M. *Surf. Sci.* **1997**, *373*, 85.

(10) Chambers, S. A.; Joyce, S. A. *Surf. Sci.* **1999**, *420*, 111.

(11) Chambers, S. A.; Thevuthasan, S.; Joyce, S. A. *Surf. Sci.* **2000**, *450*, L273.

(12) Stanka, B.; Hebenstreit, W.; Diebold, U.; Chambers, S. A. *Surf. Sci.* **2000**, *448*, 49.

(13) Anderson, J. F.; Kuhn, M.; Diebold, U.; Shaw, K.; Stoyanov, P.; Lind, D. *Phys. Rev. B* **1997**, *56*, 9902.

(14) Gaines, J. M.; Kohlhepp, J. T.; van Eemeren, J. T. W. M.; Elfrink, R. J. G.; Roozeboom, F.; de Jonge, W. J. M. *Res. Soc. Symp. Proc.* **1997**; Vol. 474, 191.

(15) Korecki, J.; Kubik, M.; Spiridis, T.; Ślęzak, T. *Acta Phys. Pol. A* **2000**, 129.

(16) Chambers, S. A. *Surf. Sci. Rep.* **2000**, *39*, 105.

(17) Handke, B.; Haber, J.; Slezak, T.; Kubik, M.; Korecki, J. *Vacuum* **2001**, *63*, 331.

(18) Handke, B. Ph.D. Thesis, unpublished.

(19) Korecki, J.; Gradmann, U. *Phys. Rev. Lett.* **1985**, *55*, 2491.

(20) Fuji, T.; Takano, M.; Katano, R.; Bando, Y. *J. Appl. Phys.* **1990**, *68*, 1735.

(21) Fuji, T.; Takano, M.; Katano, R.; Isozumi, Y.; Bando, Y. *J. Magn. Magn. Mater.* **1994**, *130*, 267.

(22) Kalev, L. A.; Schurer, P.; Niesen, L. *Phys. Rev. B* **2003**, *68*, 165407.

(23) Sawatzky, G. A.; Van der Woude, F. A.; Morish, H. *Phys. Rev.* **1969**, *183*, 383.

(24) Voogt, F. C.; Hibma, T.; Smulders, P.; Niesen, L. *J. Cryst. Growth* **1997**, *174*, 440.

(25) Korecki, J.; Handke, B.; Spiridis, N.; Slezak, T.; Flis-Kabulska, I.; Haber, J. *Thin Solid Films* **2002**, *412*, 14.

(26) Noguera, C. *J. Phys.: Condens. Matter* **2000**, *12*, R367.

(27) Hargrove, R. S.; Kündig, W. *Solid State Commun.* **1970**, *8*, 303.

(28) Mariotto, G.; Murphy, S.; Shvets, I. V. *Phys. Rev. B* **2002**, *66*, 245426.